Journal of Marine Science and Application (2026) 25: 403-422
https://doi.org/10.1007/s11804-025-00725-1

RESEARCH ARTICLE

Structural Performance of Swept Cycloidal Propeller Blades Using Coupled Boundary Element and Finite Element Method

Sreejith Kunnamkulangara[1], Anil Kumar Dash[1] and Vishwanath Nagarajan[2]

Received: 29 January 2025 / Accepted: 06 June 2025

Abstract

This study examined the impact of the leading-edge sweep angle on the vibration characteristics of a marine cycloidal propeller (MCP) blade during different ship maneuvering motions using a coupled three-dimensional boundary element method (BEM) and finite element method (FEM) approach. Through this approach, the study captured the interaction between hydrodynamics and structural dynamics, providing a comprehensive understanding of the response of the swept MCP blade. The following ship maneuvers were analyzed: bollard pull, crabbing, crash stop, cruising, and turning circle. During MCP operation, each blade undergoes one oscillation about its own longitudinal axis for each rotation of the horizontal propeller disc. The face and back of the propeller blade interchange during each oscillation. Consequently, the propeller blades are subjected to higher fluctuations in loading because of changes in the angle of attack and inflow velocity at each time instant. This results in complex and unstable fluid dynamics at the blade location. Variations in the sweep angle can profoundly influence the performance of the blade by altering the hydrodynamic loads and structural responses. The impact of the sweep angle is depicted through changes in the displacement, velocity, twisting angle, twisting moment, and von Mises stress of the blade. Furthermore, because of the load fluctuations on the blade, fatigue and load variations in each disc revolution must be considered during the design of cycloidal propellers. Therefore, a preliminary fatigue assessment for each maneuver was conducted. The research provides valuable information into the behavior of swept MCP blades under various loading conditions.

Keywords Cycloidal propeller; Ship maneuvering; Sweep angle; Boundary element method–finite element method (BEM–FEM); Fatigue

1 Introduction

A cycloidal propeller unit, unlike conventional ship propellers, is a cross-flow propeller in which thrust is generated perpendicular to the axis of rotation. Such units are used for tugs, small boats, ferries, and other marine vessels that require precise positioning and quick maneuvering. The study of fluid–structure interaction (FSI) is an important aspect of these propellers as the fluid–solid domain interaction plays a fundamental role in determining the propeller performance and efficiency. The configuration of a standard marine cycloidal propeller (MCP) mounted on a ship is shown in Figure 1. This MCP comprises six hydrofoil blades positioned vertically around a horizontal circular disc. As the circular disc rotates, each blade revolves along its own vertical axis. Throughout one revolution of the disc, pressure on each blade of MCP unit undergoes temporal variations due to blade vibration, resulting in continuous changes in the angle of attack. These fluctuations intensify during ship maneuvering because the ship maneuvers across various degrees of freedom. Hence, the fluctuating hydrodynamic forces during such maneuvers can induce high blade loads. Therefore, a thorough numerical investigation of blade loads is necessary to ensure the structural integrity and performance of the MCP. Different models of MCP units are commercially available according to the operational requirements.

In a ship, one MCP unit will be on the port side and the other unit will be in the starboard side (Prabhu et al., 2017). Despite their advantages, MCPs pose significant design challenges because of the coupling of unsteady hydrody-

Article Highlights

- Coupled Boundary Element and Finite Element Method to investigate hydro-structural dynamic interaction of Marine Cycloidal Propeller (MCP) blade under different ship maneuvering conditions.
- Effect of sweep angle on the hydrodynamic forces, displacement and stresses of the MCP blade.
- Preliminary assessment of fatigue strength of MCP blade due to hydrodynamic load fluctuations caused by rotational and oscillatory motion of MCP unit.

✉ Anil Kumar Dash
anilkumar@nitc.ac.in

[1] Civil Engineering Department, National Institute of Technology Calicut, Calicut 673601 Kerala, India

[2] Indian Institute of Technology Kharagpur, West Bengal 721302, India

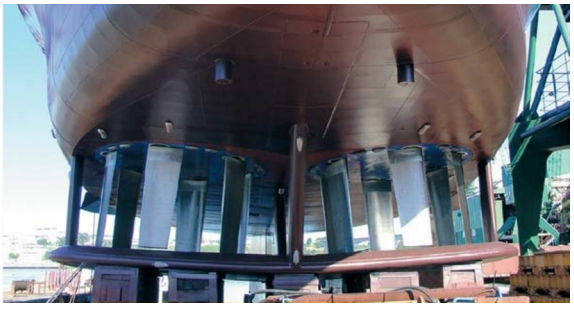

Figure 1 Typical arrangement of marine cycloidal propeller (MCP) units under a ship hull

namics and structural deformations under complex loading scenarios. Several researchers attempted to quantify these dynamics. Prabhu et al. (2017) investigated the variations in the hydrodynamic load on the propeller blade caused by steady and unsteady flow conditions using a two-dimensional (2D) panel method to calculate the lift and drag coefficient. However, they did not explore the responses and reactions of the blade due to hydrodynamic loads under different ship motions. The wide operating range of the MCP poses challenges in conducting multiple model experiments to determine the worst-case blade loading conditions. Estimating blade loading considering the maneuvering dynamics of the parent vessel creates further complications. Some studies on three-dimensional (3D) hydrofoils (Garg et al., 2017; Ducoin and Young, 2013) provided insight into the hydroelastic responses of similar structures to complex flows.

Sweep angle is generally defined as the angle made by the leading edge of the blade with its longitudinal axis. Efficient hydrofoil designs can be achieved by manipulating the influence of the sweeping of blades against or along the flow on hydrodynamic performance, thereby affecting the lift, drag, and vibration characteristics and reducing flow separations and cavitation. Hydraulic machines such as turbines and pumps adopt this approach to improve system efficiency. Sweeping aeroelastic wings are widely employed in aircraft to mitigate air flutter and static divergence. Lottati (1985) and Blair and Weisshaar (1982) attempted to mitigate the divergence of a swept-forward wing by enhancing its composite bending-torsion stiffness by adjusting fiber orientation and sweep angle. Akcabay and Young (2020) noted that blades with positive sweep angles (i.e., backward swept blades) can delay static divergence in external flows. The inflow velocity of the blades is subject to fluctuations determined by the sweep angle and relative position of the rotating disc, creating an inherently unsteady flow condition. In this context, the analysis of a swept cycloidal propeller blade presents a unique challenge owing to the intricate coupling between the fluid flow dynamics and the structural response of the blade. Liao et al. (2019) investigated how increasing the sweep angle on the leading edge reduces unsteady hydrodynamic load fluctuations on the rudder and propeller blade. It has become imperative to evaluate whether optimizing the sweep angle can enhance performance.

One of the aims of our work is to incorporate a 3D boundary element method (3D-BEM) with a finite element method (FEM) to calculate the lift coefficient and, subsequently, the hydrodynamic forces acting on the blades. The main advantage of 3D-BEM over the 2D-panel method is its ability to provide a more realistic solution by capturing and analyzing the flow field around a 3D object. Li et al. (2018) performed a hydroelastic analysis on conventional screw propellers to analyze added mass and damping using a coupled BEM–FEM algorithm. Similarly, some studies determined added mass and hydrodynamic damping of hydrofoils under different fluid dynamic conditions (De La Torre et al., 2013; Čupr et al., 2018; Kim et al., 2008; Ghassemi and Yari, 2011). Although BEM is based on the potential flow theory, certain modifications help predict unsteady flows and are comparable with computational fluid dynamics results, greatly saving simulation time. The BEM – FEM combination offers a synergistic framework for addressing the challenges posed by FSI problems. BEM, which is renowned for its capability to accurately model fluid domains and efficiently handle exterior boundary conditions, captures the fluid flow characteristics surrounding the propeller blade. Meanwhile, the FEM, which is proficient in analyzing structural behavior and handling complex geometries, characterizes the mechanical response of the propeller blade under the influence of fluid forces. There are few reports on the application of BEM–FEM coupling to marine problems. The detailed formulation of the BEM–FEM coupling is explained in further sections. MCP blades subjected to complex and cyclic hydrodynamic loads will experience fatigue. Hence, they must be designed for fatigue life as well. Recent advancements in fracture mechanics have introduced efficient numerical methods, such as the cracking elements method and its variants, effectively simulating quasibrittle and dynamic fracture without remeshing or enrichment (Wang et al., 2025; Zhang et al., 2021; Zhang and Zhuang, 2019). Since meshfree and particle-based approaches further address complex 3D crack propagation and branching (Rabczuk et al., 2010), they are suitable for fatigue and failure analysis in finite element frameworks.

In the present study, we extended the work by Prabhu et al. (2023) to analyze the impact of leading-edge sweep angle on the hydroelastic responses of the blade during various ship maneuvering motions, such as bollard pull, crabbing, crash stop, cruising, and turning circle. The study examined the effect of the leading-edge sweep angle on the displacement, velocity, twisting angle, twisting moment, and von Mises stress of the blade. The hydrodynamic normal and tangential forces acting on the blade at each time step during maneuvering were calculated by 3D BEM, and the structural dynamics were solved by nonlinear FEM. A

MATLAB code was developed for BEM–FEM coupling. The findings reveal that the effects of sweep angle have a notable impact on the response of the blade, resulting in considerable changes in stresses and deformations.

2 Problem description

The present study established the two-way coupling of 3D-BEM and FEM to improve simulation accuracy. The introduction of sweep effects further improved the responses and reactions of the propeller blades. Each ship maneuvering motion results in different hydrodynamic loadings on hydrofoil blades. Since the BEM is based on the potential flow theory, the accuracy level of this method for calculating the drag coefficient is unknown. Hence, in this work, the drag coefficient was calculated using the equation provided by the International Towing Tank Conference (ITTC). Table 1 lists the specifications of the ship and the MCP blade, which was constructed using structural steel. Figure 2 shows the coordinate systems considered to develop the mathematical formulations. The calculated hydrodynamic lift and drag forces were converted into normal and tangential components via appropriate coordinate transformation. Ship dynamics and combinations of eccentricity for various ship maneuvers were derived from Prabhu et al. (2019). In the analysis, the leading-edge sweeping of hydrofoils was maintained such that the bottom and top chords remained parallel across all sweep angles, resulting in slight variations in the effective span for higher sweep angles. Although these reductions are usually ignored, they have a considerable effect on the stiffness of the structure, and hence, they are accounted for in this work. The mass moment of inertia of the swept blade was determined numerically. Figure 3 shows the geometry and orientation of the sweep angle of the MCP blade. In this figure, a negative sign denotes a forward sweep angle of the leading edge, while a positive sign indicates a backward sweep angle.

Table 1 Ship and propeller blade characteristics

Ship length L_{PP} (m)	142
Propeller disc diameter (m)	3.6
Propeller disc speed n (r/min)	32
x-coordinate of MCP, X_P (m)	71
y-coordinate of MCP, Y_P (m)	4.5
Section of blade	NACA0024
Top chord of blade (m)	0.65
Bottom chord of blade (m)	0.52
Fixed support dimension (m)	0.26 × 0.13
Blade stock diameter (m)	0.26
Density of steel (kg/m^3)	7860

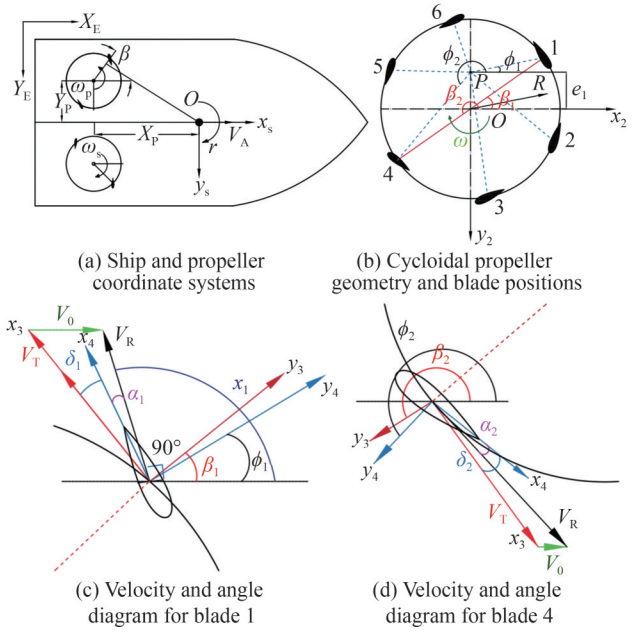

Figure 2 Coordinate systems describing the ship

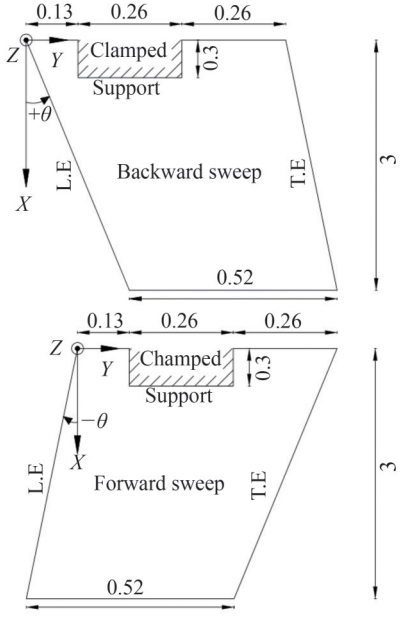

Figure 3 Sign convention for the backward sweep ($+\theta$) and forward sweep ($-\theta$) of the MCP blade (L.E: leading edge, and T.E: trailing edge)

3 Mathematical formulation

The mathematical model for ship maneuvering was sourced from Dash et al. (2012) to analyze ship motion dynamics. The hydrodynamic model for the MCP blades was taken from Prabhu et al. (2023). Subsequently, the structural dynamics aspect was examined by the FEM (Pica et al., 1980, Zienkiewicz et al., 2000). For each ship maneuvering model, inflow velocity components were the input (refer

to Table 2). The MCP hydrodynamic model then calculated the relative velocity (V_{rp}) and angle of attack (α) for each time iteration. These parameters were the input for the 3D-BEM code to calculate the velocity potential (Φ) function at the control points of the hydrofoil surface panels. The velocity potential function was used to calculate the pressure coefficient, which was transferred to the hydrodynamic model to determine the hydrodynamic lift force. Lift and drag forces were then resolved to normal and tangential components. These components were given as the input to the FEM solver and applied uniformly to the hydrofoil. After the structural equation of motion was solved, the structural responses such as displacement and twist of blade altered V_{rel} and α. Hence, for the next time instance, these parameters were updated for further simulation. Thus, the BEM and FEM solvers were coupled. The BEM–FEM coupling procedure is explained in detail in Figure 4. The computational tasks were implemented through a MATLAB code developed for this purpose.

Table 2 Ship dynamics and combination of eccentricity for different ship maneuvers

Maneuver	u (m/s)	v (m/s)	r (rad/s)	$e_{1\{S\}^{P}}$	$e_{2\{S\}^{P}}$
Bollard pull	0.772	0	0	$\begin{Bmatrix}-0.8\\0.8\end{Bmatrix}$	$\begin{Bmatrix}0\\0\end{Bmatrix}$
Crash stop	3.6	0	0	$\begin{Bmatrix}0.8\\-0.8\end{Bmatrix}$	$\begin{Bmatrix}0\\0\end{Bmatrix}$
Cruising	3.6	0	0	$\begin{Bmatrix}-0.8\\0.8\end{Bmatrix}$	$\begin{Bmatrix}0\\0\end{Bmatrix}$
Crabbing	0.772	0.257	0	$\begin{Bmatrix}-0.5\\0.5\end{Bmatrix}$	$\begin{Bmatrix}0.3\\-0.05\end{Bmatrix}$
Turning circle	$3.6\times\cos(\chi)$	$-3.6\times\sin(\chi)$	0.0076	$\begin{Bmatrix}-0.8\\0.8\end{Bmatrix}$	$\begin{Bmatrix}-0.3\\0.3\end{Bmatrix}$

Other parameters are $\chi = 20°, y_{\text{Max}} = 0.3L_{\text{pp}}, \psi_{\text{Max}} = 20°$, ω = 0.031 4 rad/s. Propeller revolution is kept the same for all maneuvers, $n_{\{S\}^{P}} = \begin{Bmatrix}-32\\32\end{Bmatrix}$ r/min.

3.1 Ship maneuvering model

Detailed model formulations of ship maneuvering are available in Prabhu et al. (2023). Hence, a brief explanation is given here. A four-degrees-of-freedom maneuvering model of a ship was used in this work. The governing equations of the motion of a ship operated with a conventional propeller are as follows:

$$\begin{aligned}
&(m+m_x)\dot{u} = (m+m_y)rv + mx_G r^2 + X_P + X_H\\
&(m+m_y)\dot{v} + (mx_G - Y_{\dot{r}})\dot{r} = -(m+m_x)ur + Y_P + Y_H\\
&(I_z + J_z)\dot{r} + (mx_G - N_{\dot{v}})\dot{v} = -mx_G ur + N_P + N_H
\end{aligned}$$

Since the MCP combines the propeller and rudder operations, some of the coefficients in the existing maneuvering mathematical model become redundant. Hence, the propeller and rudder forces and moments model are replaced by the MCP forces and moments. The input velocity components will differ for each ship maneuvering model. Further, the velocity vector at the blade location required to calculate the lift and drag forces acting on the blade is given as follows:

$$\boldsymbol{V}_{Ri\{P\}^{S}} = \begin{Bmatrix}\left[u - r\left(Y_{D\{P\}^{S}} + R\sin\theta_{Di\{p\}^{S}}\right) - \omega_{D\{P\}^{S}}\left(R\sin\theta_{Di\{P\}^{S}}\right)\right]\hat{i} +\\ \left[v + r\left(X_{D\{P\}^{S}} + R\cos\theta_{Di\{P\}^{S}}\right) + \omega_{D\{P\}^{S}}\left(R\cos\theta_{Di\{P\}^{S}}\right) - p\left(Z_{D\{P\}^{S}} + Z_{Bi\{P\}^{S}}\right)\right]\hat{j} +\\ \left[p\left(Y_{D\{P\}^{S}} + R\sin\theta_{Di\{P\}^{S}}\right)\right]\hat{k}\end{Bmatrix} \quad (1)$$

The lift and drag force on each blade can be written as shown below.

$$\begin{Bmatrix}L_{i\{P\}^{S}}\\D_{i\{P\}^{S}}\end{Bmatrix} = \begin{Bmatrix}C_{Li\{P\}^{S}}\\C_{Di\{P\}^{S}}\end{Bmatrix}\frac{1}{2}\rho A V_{Ri\{P\}^{S}} \quad (2)$$

In this work, the 3D-BEM method under unsteady flow was adopted for calculating the lift coefficient at each time instance. The drag coefficient was obtained from the ITTC (2011) recommended procedures and guidelines. A detailed explanation of the calculation of C_L is provided below. The hydrodynamic forces acting on the propeller blade are non-dimensionalized by $0.5\,\rho\, L_{\text{pp}}\, TU^2$.

3.2 Boundary element method

As inflow velocity fluctuates, the hydrodynamic flow becomes unsteady, leading to variations in the lift coefficient. The 3D-BEM is a numerical technique used to analyze fluid dynamics. However, it does not incorporate viscosity effects when calculating force coefficients. In constructing a numerical solution, the geometry is partitioned into multiple panels, each containing a control point where the panel strength is computed. The total velocity potential Φ at a control point is sum of free stream potential ϕ_∞ and perturbation

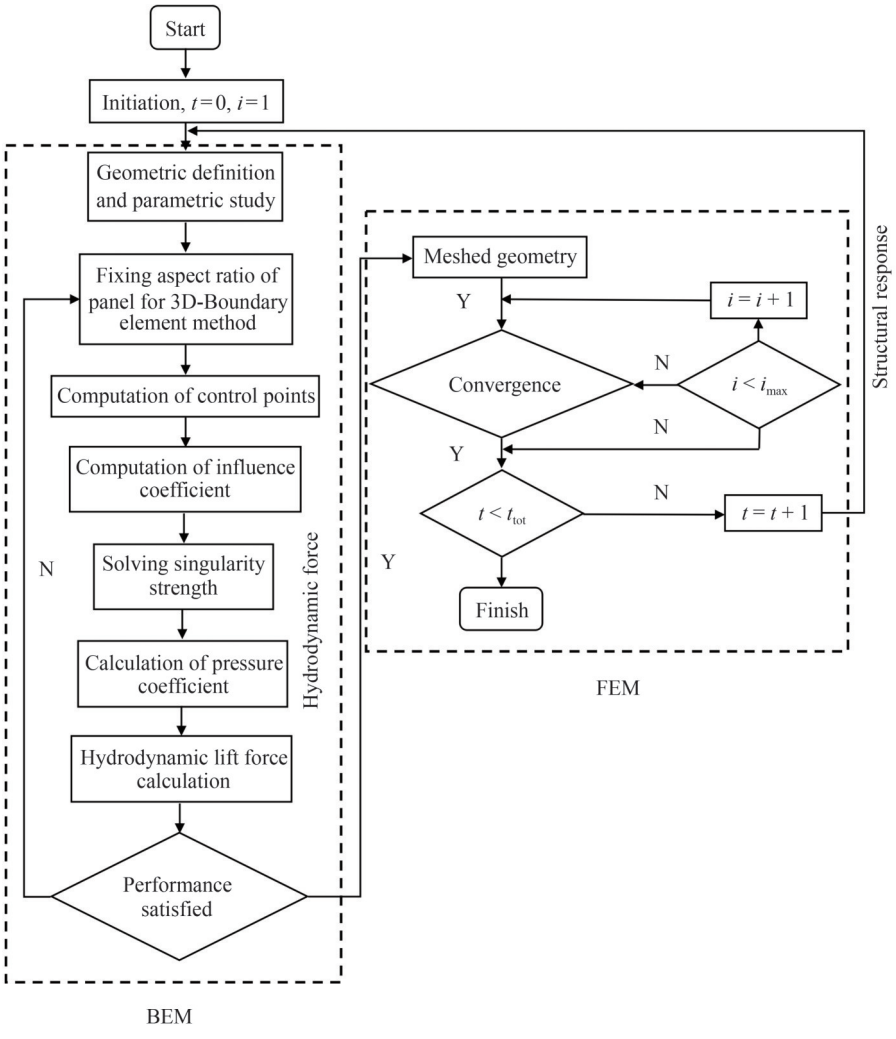

Figure 4 Schematic representation of the coupling of the boundary element method (BEM) with the finite element method (FEM)

potential $\phi(x, y, z)$ as:

$$\Phi = \phi_{\infty} + \phi(x, y, z) \tag{3}$$

This total velocity potential should satisfy Laplace's equation, $\nabla^2\Phi = 0$, in the fluid domain. It is assumed that the panel strength remains consistent within a panel but differs from the other panels. Specific conditions are enforced at each control point to address the assumption. The entire geometry is bounded by the hydrofoil surface S_h and the wake surface S_w. The perturbation potential $\phi(x, y, z)$ can be computed by applying Green's theorem to the hydrofoil surface and can be represented as a function of the source (σ) and doublet strength (μ), as illustrated below.

$$\phi(x, y, z) = \frac{1}{4\pi} \int_{S_h + S_w} \mu n \cdot \nabla\left(\frac{1}{r}\right) \mathrm{d}S - \frac{1}{4\pi} \int_{S_h} \sigma \cdot \nabla\left(\frac{1}{r}\right) \mathrm{d}S \tag{4}$$

The values of ϕ and $\frac{\partial \phi}{\partial n}$ are constant throughout a panel. The boundary conditions required to solve the given integral equation are given below:

- $\nabla^2\phi = 0$: Laplace's equation should be satisfied in the given fluid domain.
- $(\nabla\phi + v) \cdot n = 0$: The normal velocity across the solid boundaries of the body should be zero, and the kinematic velocity v at the blade surface is given as

$$v = -\left[V_{\infty} + V_{\mathrm{rel}} + \Omega \times r\right] \tag{5}$$

where V_{rel} is the relative velocity at the blade panel location; Ω is the rate rotation of the body frame of reference; n normal vector pointing out of the panel.

- $\mu_{W_{\mathrm{trail}}} = (\mu_u - \mu_l)_{\mathrm{trail}}$: This depicts the Kutta condition at the trailing edge of the boundary, where μ_u and μ_l are the doublet strength of the upper and lower panels, respectively, on the trailing edge.
- $\lim_{R \to \infty} \nabla\phi = 0$: The flow disturbance at infinity is zero.

This will provide an additional set of equations at every wake panel. The sides of these panels represent a shed vor-

tex sheet. Hence, the final integral equation can be written as follows:

$$\left\{\frac{1}{4\pi}\int_{S_h+S_w}\mu n\cdot\nabla\left(\frac{\partial}{\partial n}\left(\frac{1}{r}\right)\right)\mathrm{d}S-\frac{1}{4\pi}\int_{S_h}\sigma\cdot\nabla\left(\frac{1}{r}\right)\mathrm{d}S-V_\infty-v_{\mathrm{rel}}-\Omega\times r\right\}\cdot n=0 \tag{6}$$

For thick bodies, this condition of zero normal flow across solid boundaries can be achieved in a way that the inner perturbation potential is assumed to be constant, i.e., Φ_i = const. By selecting $\Phi_i = 0$ as the velocity potential (the problem is formulated in an inertial *XYZ* frame of reference where $\phi_\infty = 0$ and the magnitude of ϕ corresponds to the perturbation potential in a steady-state flow), the following equation can be written.

$$\frac{1}{4\pi}\int_{S_h+S_w}\mu\cdot\frac{\partial}{\partial n}\left(\frac{1}{r}\right)\mathrm{d}S-\frac{1}{4\pi}\int_{S_h}\sigma\cdot\left(\frac{1}{r}\right)\mathrm{d}S=0 \tag{7}$$

In the above equation, dipole strength μ and source strength σ are the only unknowns. The source strength can be written as $\sigma = -[V_\infty + V_{\mathrm{rel}} + \Omega \times r]\cdot n$ (Katz and Plotkin, 2001). The entire geometry is discretized into a number of surfaces (N) and wake panels (N_W). Figure 5 shows the surface panel distribution for the 3D-BEM on the propeller blade.

The control point of the ith panel is influenced by all k body panels and l wake panels as follows:

$$\sum_{k=1}^{N}C_{ik}\mu_k+\sum_{l=1}^{N_w}C_{il}\mu_l+\sum_{k=1}^{N}B_{ik}\sigma_k=0 \tag{8}$$

where $C_{ik}=\frac{1}{4\pi}\int_{1,2,3,4}\frac{\partial}{\partial n}\left(\frac{1}{r}\right)\mathrm{d}S\big|_k$ and $B_{ik}=-\frac{1}{4\pi}\int_{1,2,3,4}\left(\frac{1}{r}\right)\mathrm{d}S\big|_k$ are the influence coefficients of panel k defined by four corners (labeled 1, 2, 3, and 4). A panel representation of the NACA 0024 hydrofoil is shown in Figure 6. The strength of all wake panels can be linked to the unknown upper and lower doublet strength values at the trailing edge through the Kutta condition. Hence, by further reducing the above-mentioned equation for the first-time step (at $t = \Delta t$), we get the following:

$$\sum_{k=1}^{N}A_{ik}\mu_k+\sum_{k=1}^{N}B_{ik}\sigma_k=0 \tag{9}$$

In an unsteady potential flow, wake generation and evolution are essential for conserving the circulation and satisfying the Kutta condition at the trailing edge. When a lifting body such as a propeller blade generates lift, it sheds a trailing vortex sheet into the wake, which induces an associated drag force known as induced drag. This is because the presence of a vortical wake alters the flow field—hence, the blade can no longer be treated as an isolated body in an undisturbed flow (Ozdemir and Barlas, 2021). The wake sheet is treated as a zero-thickness surface, aligned with the relative velocity, and its sides represent the shed vortex sheet, which dynamically interacts with the flow field. Hence, the present model allows the wake panel to evolve under the influence of local flow and blade motion.

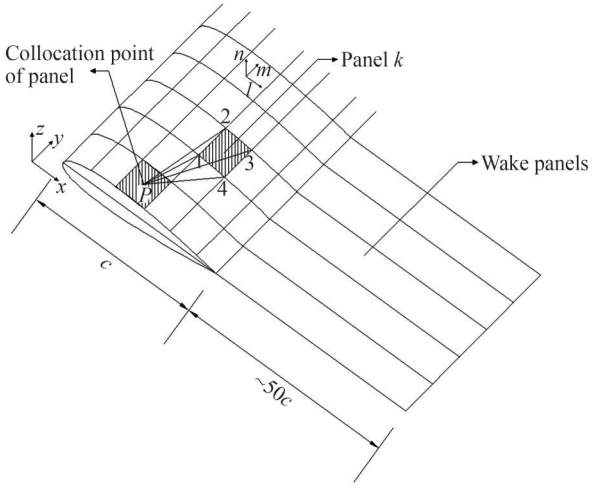

Figure 5 The panel local coordinate system for evaluating the tangential velocity components

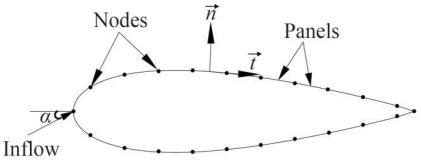

Figure 6 Panel representation of NACA 0024 hydrofoil

The above sets of equations can be solved by the Gaussian elimination method. The matrix form of the above sets of integral equations after geometric discretization is given as follows:

$$\begin{pmatrix} A_{1,1} & A_{1,2} & \rightarrow & \rightarrow & A_{1,N} & A_{1,N+1} \\ A_{2,1} & A_{2,2} & \rightarrow & \rightarrow & A_{2,N} & A_{2,N+1} \\ \downarrow & \downarrow & \downarrow & \downarrow & \downarrow & \downarrow \\ \downarrow & \downarrow & \downarrow & \downarrow & \downarrow & \downarrow \\ A_{N,1} & A_{N,2} & \rightarrow & \rightarrow & A_{N,N} & A_{N,N+1} \end{pmatrix}\begin{pmatrix}\mu_1\\ \mu_2\\ \downarrow\\ \downarrow\\ \mu_N\end{pmatrix}=\begin{pmatrix}\mathrm{RHS}_1\\ \mathrm{RHS}_2\\ \downarrow\\ \downarrow\\ \mathrm{RHS}_N\end{pmatrix} \tag{10}$$

After the perturbation potential is calculated, the perturbation velocity component in the l direction can be formulated as $q_l=\frac{1}{2\Delta l}(\mu_{l+1}-\mu_{l-1})$. The total velocity at each control point of the panel is the sum of the kinematic velocity and the perturbation velocity:

$$V_k = \left[v_l(t), v_m(t), v_n(t)\right]_k \cdot (l, m, n)_k + \left(q_{l,} q_{m,} q_k\right)_k \quad (11)$$

By using the above mathematical expressions provided, a MATLAB code was created to analyze the hydrofoil geometry under investigation to ascertain the variations in the lift coefficient. The geometry was discretized into a 35 × 11 surface panel grid. Control point coordinates were derived by averaging the vertices of each panel. Subsequently, the area vector and outward normal vector of each panel were computed based on these position vectors. Thereafter, the velocity potential function was established for each panel section. The pressure coefficient was calculated using the Bernoulli equation:

$$C_p = 1 - \frac{V_k^2}{V_{rp}^2} - \frac{2}{V_{rp}^2}\frac{\partial \phi}{\partial t} \quad (12)$$

where $V_{rp} = -\left[V_\infty + \Omega \times r\right]$. The lift coefficient was then calculated, as shown below, by rotating the pressure coefficients by the angle of attack. The empirical formula for the drag coefficient was obtained from the ITTC-recommended procedures and guidelines (ITTC, 2011):

$$C_L = C_{PZ}\sin\alpha - C_{PX}\cos\alpha \quad (13)$$

$$C_D = 2\left(1 + 2\frac{\text{th}}{c}\right)\frac{0.075}{(\log_{10}Re - 2)^2} \quad (14)$$

where Re is the Reynolds number, and th and c are the thickness and chord length of the NACA hydrofoil section, respectively.

3.3 Fluid–structure interaction

The dynamic equilibrium equation for the geometrically nonlinear behavior of the MCP blade is $M\ddot{U}_{t+\Delta t} + C\dot{U}_{t+\Delta t} + N_{t+\Delta t} = F_{t+\Delta t}\left(U, \dot{U}, t\right)$. Here, M includes the mass of the structure and added mass; C includes structural and hydrodynamic damping; $N_{t+\Delta t}$ is the equilibrated internal elastic force $\left(N_{t+\Delta t} = N_t + \left(K_T\right)_t \delta U\right)$ at time $t + \Delta t$; and $F_{t+\Delta t}\left(U, \dot{U}, t\right)$ is the nonlinear hydrodynamic load at time $t + \Delta t$, and it depends on the displacement and velocity of structure. $\delta U = U_{t+\Delta t} - U_t$, $\left(K_T\right)_t$ is the tangent stiffness at time t. N_t is the equilibrated internal elastic force $\left(N_t = KU_t\right)$ at time t, and K is the structural secant stiffness matrix. If the solution is known at time t, then the following increment of equilibrium equations is considered to calculate the response at time $t + \Delta t$. The implicit Newmark-β method was used to obtain the time integration solution of nonlinear dynamic equations. The discrete time increment (Δt) for the numerical integration was taken as 0.005 s. During maneuvering motions, the ship dynamics also influence the flow to the propeller. The displacement, velocity, and acceleration of the blade were calculated in each time step. Once the displacement is known, the strain and stress can be calculated in sequence. At each node, there were five degrees of freedom (u_x, u_y, u_z, θ_x, θ_y) and five reactions (F_x, F_y, F_z, M_x, M_y). The reactions of the support were obtained by the vector addition of the forces and moments at the support nodes. Drag is the support force in the Y direction, whereas lift is the support force in the Z direction. The support moment in the X direction is a bending moment, whereas that in the Y direction is the torque on the propeller blade shaft. The XYZ is the fixed coordinate system of the blade. The angular rotation of the MCP blade and disc creates an unsteady flow. The inflow to the blade also changes with the blade orbit angle on the disc. At each time instance, the axial rotation of the blade (ε_y) causes the angle of attack (α) to vary along the span of the propeller blade. The angle of attack is influenced by the twisting angle of the blade as follows:

$$\alpha_{t+\Delta t} = \alpha_t + \theta_y \quad (15)$$

The distance between the blade and the center of the disc (R_d) changes along the span because of vibration. Hence, at each time instance, the radial distance of the blade from the axis of the disc is given as follows:

$$\left(R_d\right)_{t+\Delta t} = \left(R_d\right)_t + U_Z \quad (16)$$

Further, the vibration velocity ($\vec{\dot{U}}$) alters the velocity at the blade location at each time instance:

$$(\vec{V}_{\text{RB}i})_{t+\Delta t} = (\vec{V}_{\text{RB}i})_t + \vec{\dot{U}} \quad (17)$$

These equations provide a BEM–FEM coupled effect, and accordingly, further reactions and responses of the blade can be calculated.

4 Results and discussion

We analyzed the dynamic responses of MCP blades at different sweep angles during various ship maneuvering motions. We examined the responses, including displacement, velocity, twisting angle, twisting moment, and von Mises stress, during maneuvers such as bollard pull, crabbing, crash stop, cruising, and turning circle. For each maneuver, the normal and tangential components of the force acting on the blade were computed. Forces and moments at the support of blade no. 1 for the port propeller were calculated in the fixed coordinate system of the blade. The sweep angle varied from −10° to +10°. Here, the positive angles indicate backward sweeps, and negative values represent forward sweep angles. Altering the sweep angle of the leading edge changes the effective span of the blade, causing variations in its mass moment of inertia (Figure 7).

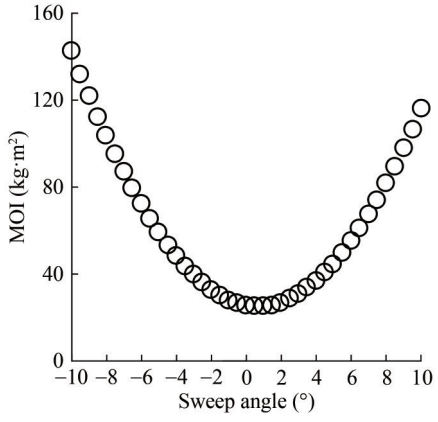

Figure 7 Variations in the mass moment of inertia of the blade with the sweep angle

4.1 Free vibration of the MCP blade

The FEM code can predict the structural response of an MCP blade during different ship maneuvers. A mesh convergence analysis was conducted to examine the free vibration of the blade. In this case, 3D-BEM was not applied since no hydrodynamic force acted on the structure. The variations in the first natural frequency with increasing mesh size are shown in Figure 8, with mesh convergence achieved at 4 500 elements. The free vibration analysis of the MCP blade was performed under in-air conditions using a MATLAB code and under in-water conditions using the acoustic module of ANSYS across a range of sweep angles at the leading edge from −10° (forward) to +10° (backward).

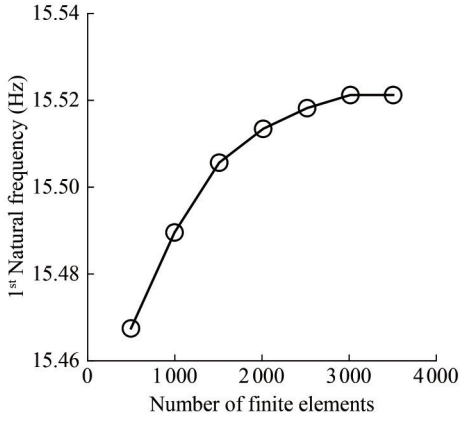

Figure 8 Mesh convergence study of the first natural frequency

The 3D-BEM code was developed to calculate the hydrodynamic forces acting on the blade during different ship maneuvers. For validation, a 3D NACA 0012 airfoil (spans 5 and 10 m) was developed, and lift coefficients with different angles of attack were calculated and compared (Figure 9). The entire geometry was divided into 50 sections along the chord and 20 sections along the span to avoid extreme values of the aspect ratio of the panels. The results showed good agreement with the published literature (Ozdemir and Barlas 2021). Notably, the theoretical models and control strategies employed in this study were previously validated through extensive model experiments. Details of the experimental setup and results can be found in our earlier works (Nandy et al., 2022; Nandy et al., 2018). Figure 10 shows the variations in the first four natural frequencies of the MCP blade in air and water at different sweep angles. The added mass effect causes a significant reduction in natural frequency across all mode shapes. The natural frequency diminishes with an increase in sweep angle, whether forward or backward. Symmetrical variations in mode shapes were observed for both forward and backward sweeps. The physical length of the blade may vary because of changes in the sweep angle, thereby affecting element size; this aspect is duly considered in this study. While maintaining an overall division based on span and chord, adjustments for the aforementioned effect on the element size were made accordingly.

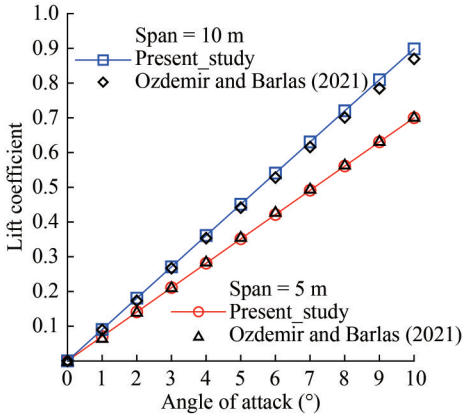

Figure 9 Comparison of lift coefficients with different angles of attack of inflow from Ozdemir and Barlas (2021) and the present study for 3D airfoil

4.2 Bollard pull

Bollard pull is a critical measure in ship maneuvering, particularly for tugs and other work vessels. It represents the maximum force that a ship can exert while remaining stationary. It is typically measured by securing the vessel to a fixed bollard on the dock and recording the force exerted by its propulsion system. This measurement is essential for assessing the capability of a vessel to perform tasks such as towing or pushing other ships and objects. Choosing the optimum element size for FEM and BEM is important for the numerical simulation since this size influences the results. Three grid combinations (coarse, medium, and fine) were considered for the convergence study. The refinement of multiple grids was uniform or nonuniform. For uniform grid refinement, the grid refinement ratio was $r_G = h_2/h_1 = h_3/h_2$, where h_3, h_2, and h_1 denoted the grid spacing of the

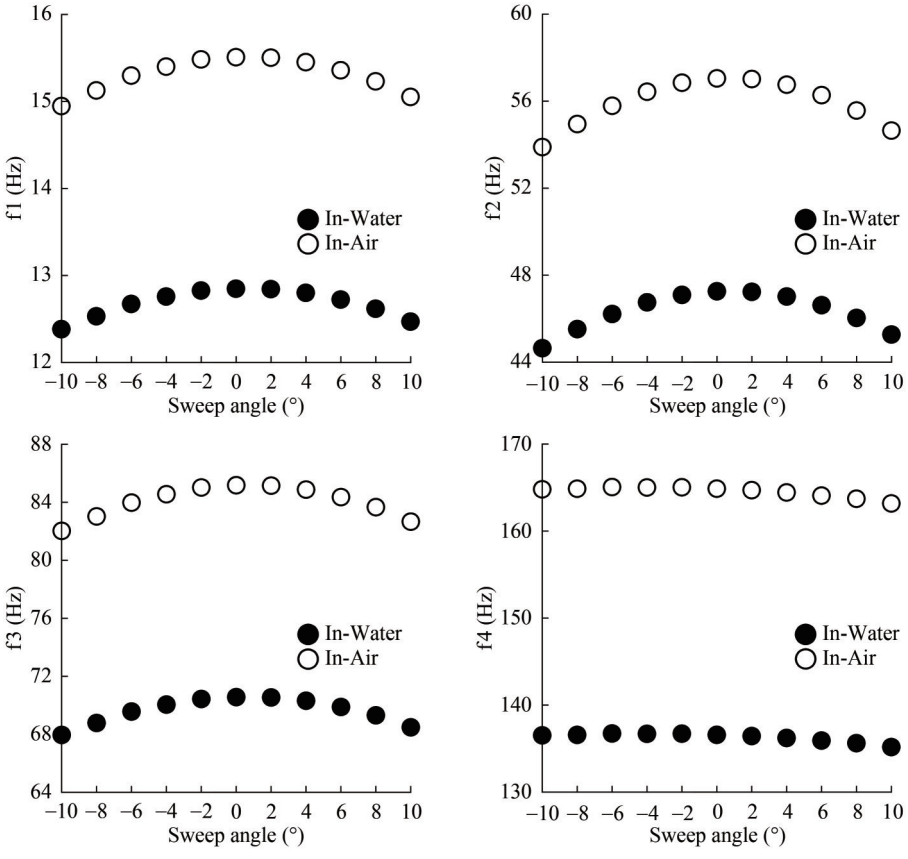

Figure 10 Comparison of the natural frequency of the MCP blade in air and in water (f1–f4: first–fourth modes)

coarse, medium, and fine grids, respectively. For nonuniform grid refinement, the grid refinement ratio was $r_{G21} = h_2/h_1$, and $r_{G32} = h_3/h_2$. By considering the difference between the coarse and medium grid solutions $\varepsilon_{G32} = |S_3 - S_2|$ and the difference between the medium and fine solutions $\varepsilon_{G21} = |S_2 - S_1|$, the grid convergence ratio R_G was calculated as $R_G = \varepsilon_{G21}/\varepsilon_{G32}$. Based on the R_G value, the state of discretization convergence can be classified as follows:

i) Monotonic convergence (mon.): $0 < R_G < 1$

ii) Oscillatory convergence (osc.): $R_G < 0$ and $|R_G| < 1$

iii) Monotonic divergence (div.): $R_G > 1$

iv) Oscillatory divergence (div.): $R_G < 0$ and $|R_G| > 1$

If condition i) is satisfied, grid convergence is achieved. The convergence is monotonic convergence, meaning that the solution approaches a value asymptotically when the grid is refined.

Table 3 lists the convergence analysis results of the MCP blade. The tip displacement difference between medium and fine grids is only 0.70%, indicating convergence. The medium mesh grid was selected for the analysis as it provided a balance between accuracy and computational efficiency, meeting convergence criteria within 1%. We adopted 3D hexahedral structural meshing (Figure 11) with 1 812 elements and 10 483 nodes. A comparison of the results obtained with the present MATLAB code for FEM with the ANSYS results for displacement and von Mises stress of the MCP blade at a sweep angle of 1.24° during bollard pull ship maneuvering is shown in Figure 12. The hydrodynamic forces acting on the MCP blade were calculated by the BEM and used as an input force in ANSYS software. A transient analysis simulation was performed, the results from numerical simulations and software solutions are compared. The present results obtained with the MATLAB code for FEM show good agreement with the ANSYS results.

Table 3 Convergence analysis for the FEM–BEM simulation

Mesh grid type	Finite mesh size (Elements)	Grid refinement ratio (R_{G1})	Surface panel count (BEM)	Grid refinement ratio (R_{G2})	Solution (S)	Error (ε_G)	R_G
Coarse (h_3)	2600	0.86	280	0.73	0.00830	0.00025	0.24
Medium (h_2)	3000		385		0.00855		
Fine (h_1)	4500	0.67	560	0.69	0.00861	0.00006	

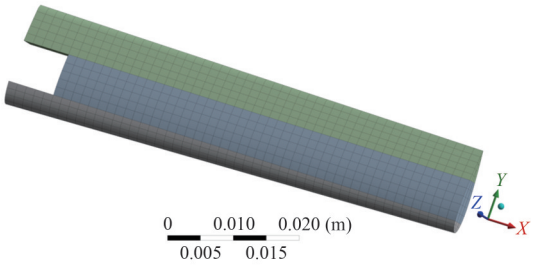

Figure 11 Meshed geometry of the MCP blade modeled in ANSYS

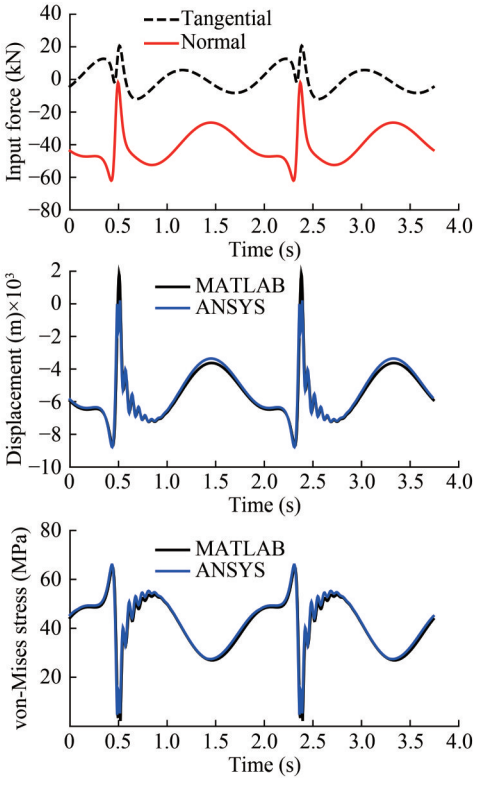

Figure 12 Validation of the present MATLAB code for FEM with ANSYS (2023) results of displacement and von Mises stress of the MCP blade at a sweep angle of 1.24° during bollard pull ship maneuvering. Top (normal and tangential hydrodynamic force), middle (tip displacement of the blade), and bottom (von Mises stress generated at the support)

Variations in the dynamic responses and strength of the MCP blade with sweep angle during bollard pull ship maneuvering are shown in Figure 13. The maximum amplitudes of the normal and tangential forces are 62 kN and 55 kN, respectively, for each cycle of disc rotation. The forces operating on the propeller are probably caused by the unstable flow conditions during bollard pull, characterized by high thrust and low forward speed. The results indicate that the sweep angle notably affects blade displacement. With increasing backward sweep, the blade tip displacement increases by 0.032 m per degree, while increasing the forward sweep results in a decrease of 0.017 m per degree. This asymmetry can be attributed to the combined effects of blade geometry and the direction of water flow relative to the sweep angle. Changes in the sweep angle do not cause any significant changes in the velocity and twisting angle of the blade. This result suggests that the sweep angle primarily affects the bending response of the blade.

The von Mises stress was analyzed to assess the structural integrity of the blade. The stress was minimal for the unswept configuration and increased with forward and backward sweep. For the forward sweep, the stress increased linearly, suggesting a consistent relationship with the sweep angle. In contrast, it increased quadratically with the backward sweep, indicating a more intricate relationship between the resulting blade loads and the sweep angle. Notably, the maximum stress remained within the yield stress of the blade material, implying no plastic deformation. The trend of the twisting moment was similar to that of displacement. The twisting moment increased by 0.21 kN·m per degree backward sweep and decreased by 0.16 kN·m per degree forward sweep. The higher twisting moment in the backward sweep was likely due to the increased leverage of the swept blade tip relative to the rotational axis. The hydrodynamic normal force decreased with increasing sweep angle for both forward and backward sweeps; however, the force was higher in the backward sweep. This trend can be explained by the varying angle of attack experienced by the blade sections at different sweep angles. The quadratic relationship suggests a nonlinear effect of sweep angle on the force generation mechanism. The time series plot of von Mises stress at a node of the MCP blade where the maximum von Mises stress occurs at sweep angles of −10°, 0°, and +10° during bollard pull maneuvering is shown in Figure 14. Unsteadiness in the flow causes a sudden change in stress magnitude within a very short interval of time. The contour plots shown in Figure 15 further illustrate the significant variations in stress along the blade span and chord, particularly near the support. The location of the maximum stress also shifts with the sweep angle, moving toward the trailing edge for backward sweep, centering at zero sweep, and reaching the leading edge for forward sweep. This movement reflects the changes in the load distribution on the blade with the sweep angle.

4.3 Crabbing

Crabbing is a ship maneuvering technique used to move a vessel sideways without changing its heading considerably. This maneuver is particularly useful for docking, undocking, or navigating in tight spaces such as narrow channels or crowded harbors. During crabbing, the ship employs MCP blades to generate lateral forces that move the vessel perpendicular to its longitudinal axis. The nondimensionalized hydrodynamic normal and tangential forces and displacement on the MCP blade during crabbing are shown in Figure 16. The normal component of force does not change with disc rotation. However, the tangential force compo-

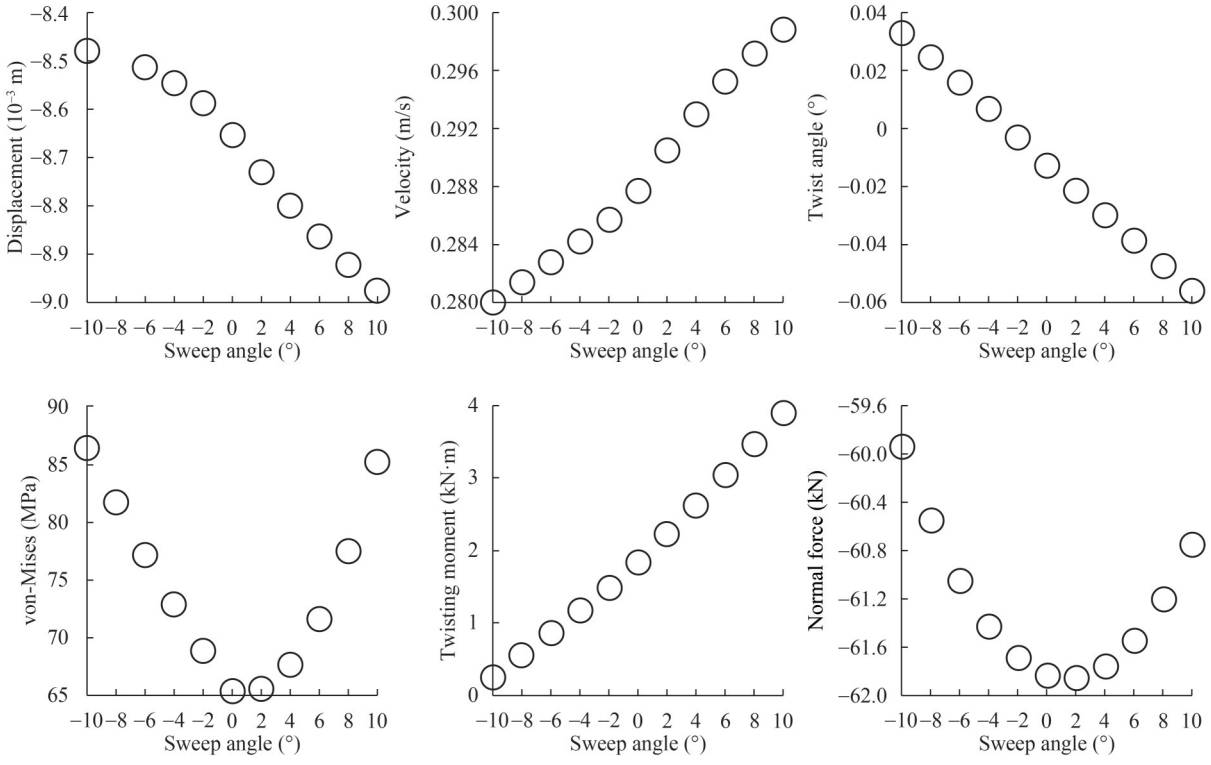

Figure 13 Variations in maximum displacement, velocity, twist angle, twisting moment, von Mises stress, and normal force with changes in the sweep angle for the MCP during bollard pull maneuvering

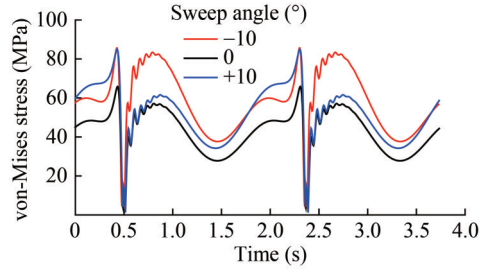

Figure 14 Time series plot of the von Mises stress at the node of the MCP blade where the maximum von Mises stress occurs at sweep angles of −10°, 0°, and +10° during bollard pull maneuvering

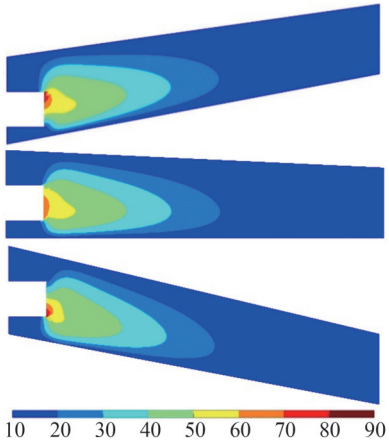

Figure 15 Contour plot of the von Mises stress on the MCP blade at the time of the maximum von Mises stress during bollard pull maneuvering

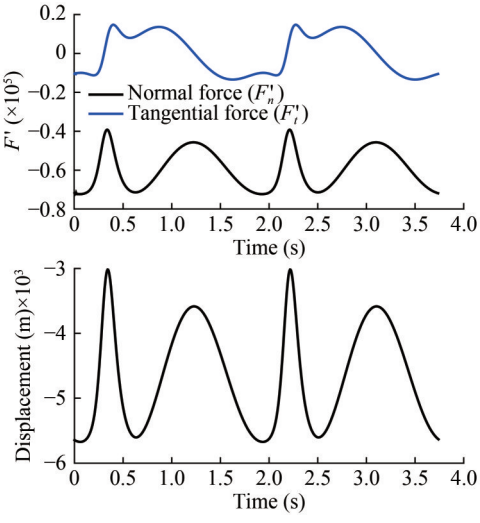

Figure 16 Nondimensionalized hydrodynamic normal and tangential forces acting on the MCP and displacement on the MCP under the unswept (0° sweep angle) condition during crabbing

nent changes from positive to negative and vice-versa for each disc rotation. The maximum normal and tangential force components experienced by the blade reach 42 and 8.5 kN, respectively. Variations in dynamic responses and strength of the MCP blade during crabbing are shown in Figure 17. Backward sweep increases blade displacement by 0.022 m per degree, while forward sweep decreases it by 0.010 m per degree. This asymmetry is attributed to the

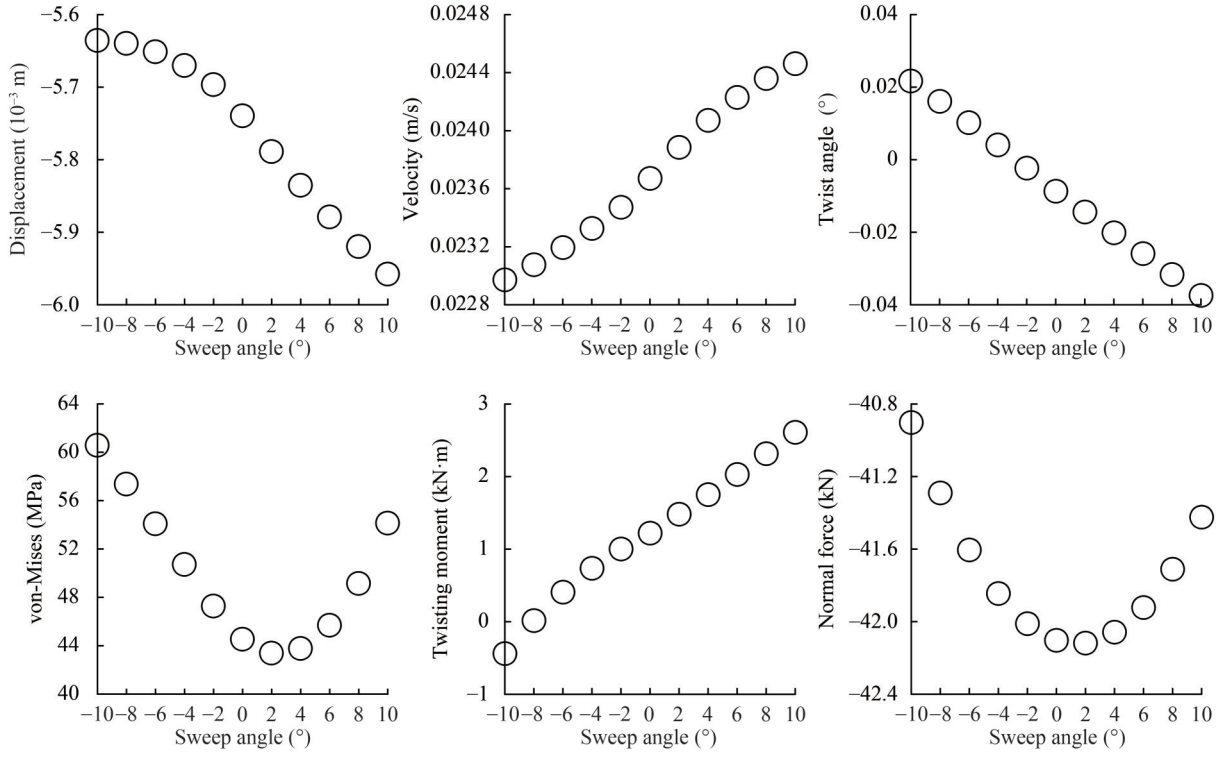

Figure 17 Variations in the maximum displacement, velocity, twist angle, twisting moment, von Mises stress, and normal force with changes in the sweep angle for the MCP during crabbing

interplay between blade geometry and water flow direction relative to the sweep angle. Variations in sweep angle cause minimal variations in blade velocity and twisting angle, suggesting that the blade velocity and twisting angle are primarily influenced by the bending response of the blade.

The von Mises stress is minimal at a sweep angle of 2° and increases with both forward and backward sweep. The increase follows a linear trend for the forward sweep, indicating a predictable relationship. However, a parabolic increase is observed with increasing backward sweep, suggesting a more complex interaction between the sweep angle and the resulting blade loads. The maximum stress remains within the safe limits of the blade material. The twisting moment increases with the backward sweep and decreases with the forward sweep. This difference can be attributed to the varying thrust forces experienced by the propeller during crabbing.

The hydrodynamic normal force decreases with increasing sweep angles for the forward and backward sweep, though the force is higher for the backward sweep. This can be explained by the varying angles of attack on different blade sections at different sweep angles. The observed quadratic relationship suggests a nonlinear effect of the sweep angle on the lateral force generation mechanism. The absence of significant stress fluctuations during crabbing, as seen from the time series plots given in Figure 18, highlights the steadier flow conditions compared to bollard pull maneuvering. The contour plots shown in Figure 19 further illustrate the significant variations in stress along the blade span and chord, particularly near the support. The location of maximum stress also shifts with the sweep angle, moving toward the trailing edge for a backward sweep, centering at zero sweeps, and reaching the leading edge for a forward sweep. This movement reflects the changing load distribution on the blade due to the sweep angle. Overall, this analysis demonstrates that crabbing maneuvers induce distinct forces, displacements, and stress patterns on the MCP blade. These insights are useful for improving blade design and comprehending the structural loads involved.

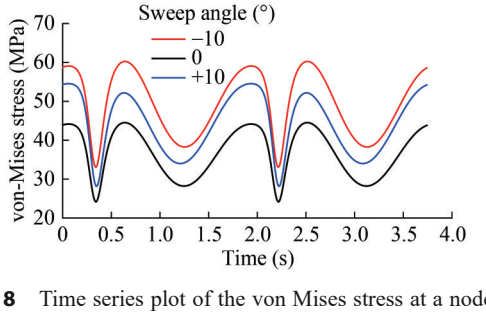

Figure 18 Time series plot of the von Mises stress at a node of the MCP blade where the maximum von Mises stress occurs at different sweep angles during crabbing

4.4 Crash stop

A crash stop is an emergency ship maneuver used to bring a vessel to a rapid halt. This procedure is typically

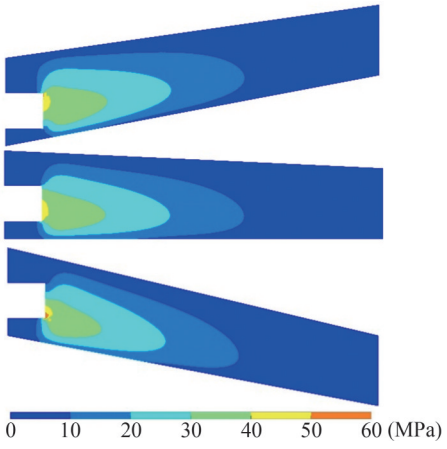

Figure 19 Contour plot of the von Mises stress on the MCP blade at the time when the maximum von Mises stress occurs during crabbing

employed to avoid collisions or to stop the ship in critical situations. During a crash stop, the ship's engines are reversed at full power, creating a strong reverse thrust that counteracts the vessel's forward momentum. These maneuvers present a distinct set of challenges for the MCP blades compared to crabbing and bollard pull maneuvers. The substantial forces required for rapid deceleration are evident in the high normal force reaching 179 kN, exceeding those observed in crabbing, as shown in Figure 20. Furthermore, the tangential force also exhibits a significant magnitude (206 kN) and alternating sign because of the rapid propeller pitch reversal during the crash stop. Variations in the dynamic responses and strength of the MCP blade during crash stop are shown in Figure 21. Backward sweep results in a higher blade displacement and velocity than the forward sweep, likely because of the interplay between blade geometry, water flow, and the increased loads experienced during crash stop. The twisting angle also

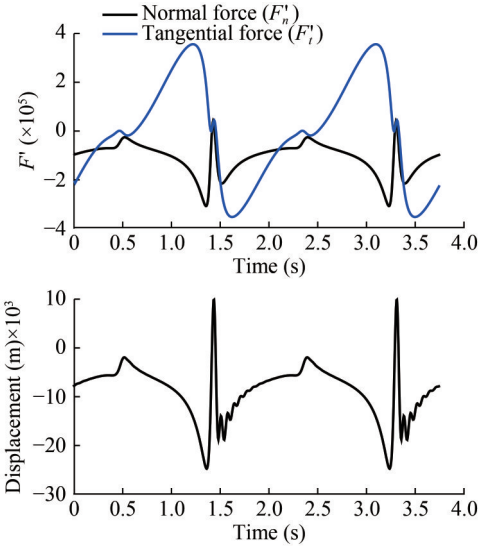

Figure 20 Nondimensionalized hydrodynamic normal and tangential force components and displacement on the MCP under unswept (0° sweep angle) conditions during the crash stop process

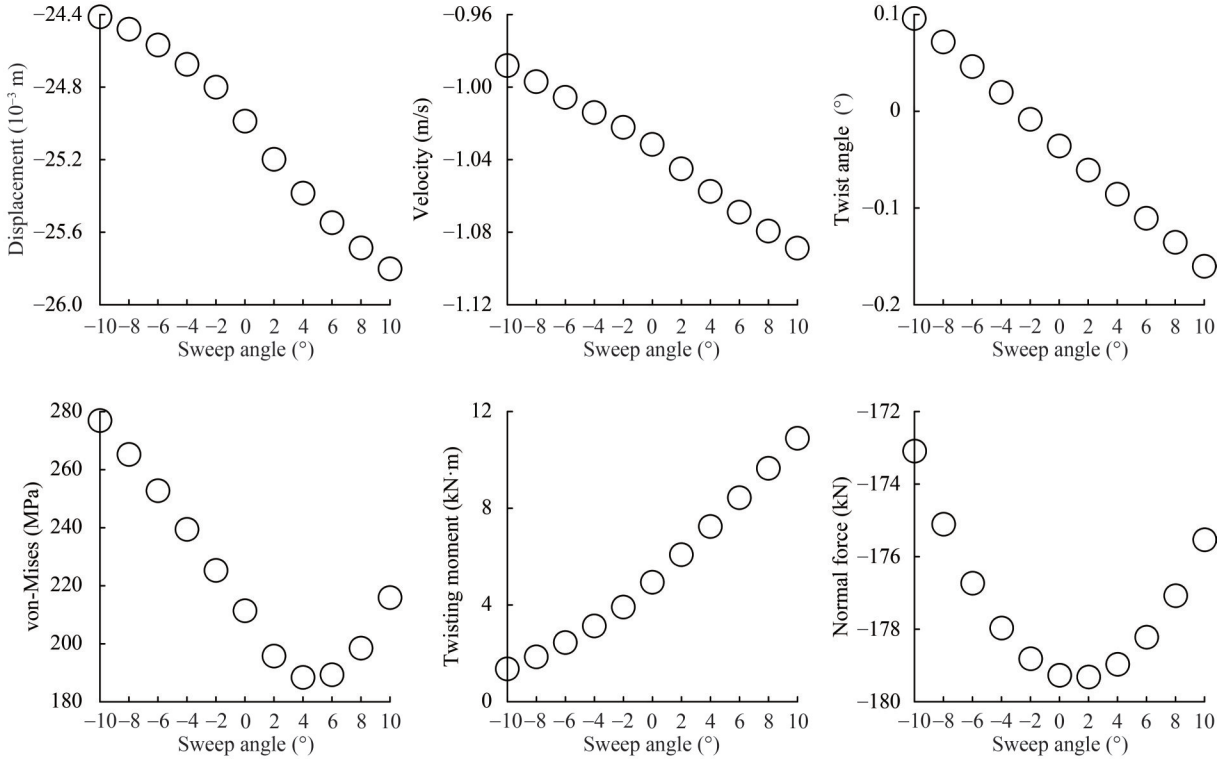

Figure 21 Variations in maximum displacement, velocity, twist angle, twisting moment, von Mises stress, and normal force with changes in the sweep angle of the MCP during the crash stop process

exhibits sweep angle dependence and the minimum value is observed at −2° sweep. An important aspect of crash stop is the high stress developed on the blade. The von Mises stress exceeds the yield stress of the blade material, suggesting potential for permanent deformation (Figures 22 and 23). The stress follows a linear trend for the forward sweep but exhibits a more complex parabolic increase for the backward sweep. The twisting moment also increases with the backward sweep and agrees with the observed increase in tangential force.

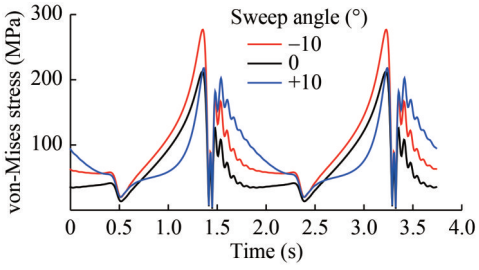

Figure 22 Time series plot of the von Mises stress at a node of the MCP blade where the maximum von Mises stress occurs at different sweep angles during the crash stop process

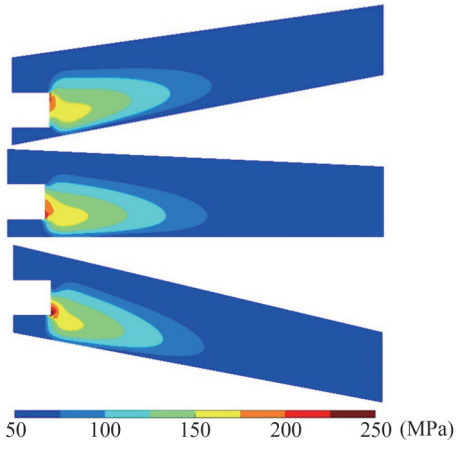

Figure 23 Contour plot of the von Mises stress on the MCP blade at the time when the maximum von Mises stress occurs during the crash stop process

The normal force for deceleration decreases with increasing sweep angle but remains higher in the backward sweep. This can be attributed to the varying angles of attack experienced by different blade sections. In contrast to the more stable flow conditions encountered during crabbing, crash stop involves notable stress changes, as seen from the time series plots. In contrast to crabbing, where the range is less (0–60 MPa), the stress distribution pattern in crash stop varies along the blade span and chord (50–250 MPa). In conclusion, crash stop maneuvers induce considerably higher forces, displacements, and stresses on the MCP blade. The results highlight the critical role of strong blade design and cautious handling techniques in reducing the risk of structural damage in emergency scenarios where the blade is subjected to loads that are greater than its material limitations.

4.5 Cruising

Cruising is the motion of a ship in a straight direction with a particular velocity. This operation does not require sudden changes in direction and velocity, and conventional screw propellers are efficient for this operation. MCP units also provide sufficient stability and thrust for this operation. Compared to crabbing and crash stop maneuvers, cruising presents a different set of demands for the MCP blade. For instance, the normal force responsible for thrust reaches a maximum of 27 kN, and similar to other maneuvers, the direction of this normal force remains relatively constant throughout the propeller rotation. The tangential force is also moderate (22 kN) and alternates in sign with each rotation cycle. The variations in the dynamic responses and strength of the MCP blade during cruising are shown in Figure 24. Backward sweep increases blade displacement, while forward sweep shows a more intricate relationship. This suggests the effect of sweep angle on blade deflection depends on its direction. Changes in blade velocity and twisting angle are minimal, with variations in sweep angle during cruising. The stress on the blade during cruising is also moderate and is within the safe limits of the blade material (Figures 25 and 26). Similar to other maneuvers, the von Mises stress during cruising is minimal at a 2° sweep angle and increases for both forward and backward sweep. The increase follows a linear trend for the forward sweep and a parabolic trend for the backward sweep. The twisting moment increases with the backward sweep and decreases with the forward sweep. The normal force contributing to forward thrust, similar to that

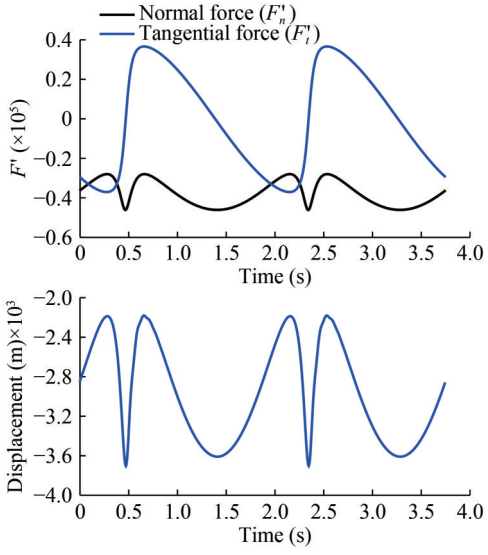

Figure 24 Nondimensionalized hydrodynamic normal and tangential forces acting on the MCP in the unswept (0° sweep angle) condition during cruising

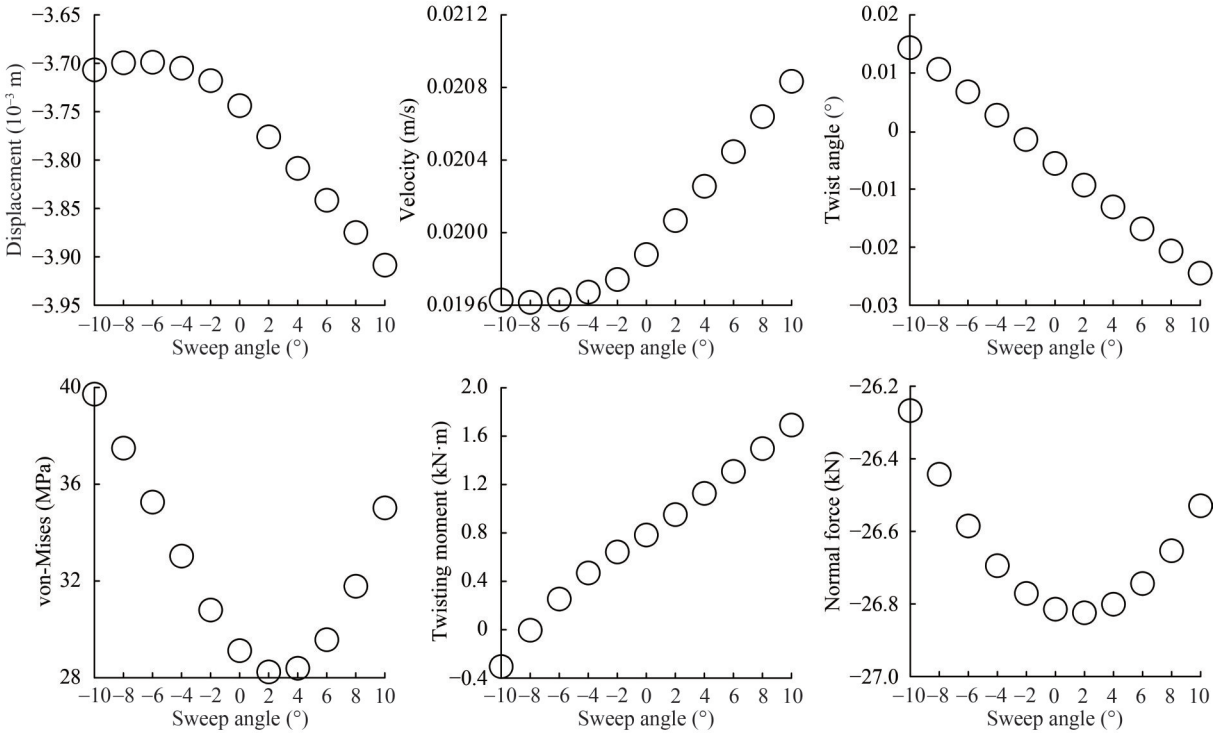

Figure 25 Variations in the maximum displacement, velocity, twist angle, twisting moment, von Mises stress, and normal force with changes in the sweep angle for the MCP during cruising

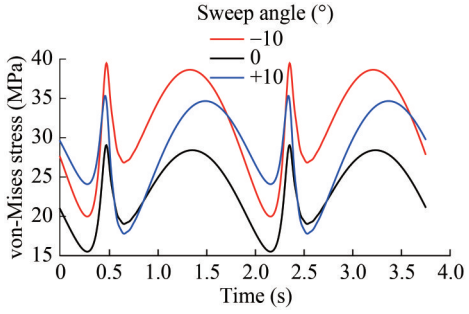

Figure 26 Time series plot of the von Mises stress at a node of the MCP blade where the maximum von Mises stress occurs at different sweep angles during cruising

in other maneuvers, decreases with increasing sweep angle in both directions. However, the force remains higher in the backward sweep. This can be explained by the varying angles of attack on different blade sections at different sweep angles, as observed in crabbing and crash stops. From the time series plots, we can infer that stress fluctuations are less significant in cruising compared to crash stop due to the steadier flow conditions during steady forward motion in the former. The stress distribution pattern shown in Figure 27 exhibits variations along the blade but with a lower stress range (5–40 MPa) compared to crabbing and crash stop. In conclusion, cruising maneuvers induce moderate forces, displacements, and stresses on the MCP blade. The blade operates within safe stress limits during cruising, highlighting the contrasting demands placed on it during different ship maneuvering operations.

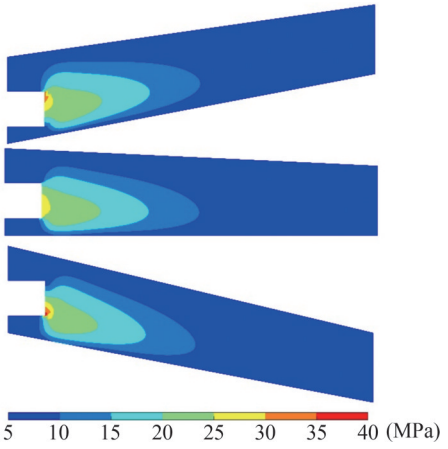

Figure 27 Contour plot of the von Mises stress on the MCP blade at the time when the maximum von Mises stress occurs during cruising

4.6 Turning circle

Turning circle is the process by which a ship executes a full 360° turn, and it is crucial in evaluating the handling characteristics and overall maneuverability of the ship. The maneuver is typically performed both to the port (left) and starboard (right) to assess the handling of the ship on both sides. When turning, the ship experiences various hydrodynamic forces, including lateral and centrifugal forces, which affect its stability and heeling. Both involve moder-

ate forces, with the normal force reaching a maximum of 27 kN, which is substantially lower than that experienced in crabbing or crash stops. Similar to other maneuvers, the normal force direction remains constant throughout propeller rotation. The tangential force is also moderate (23 kN) and alternates in sign with each rotation cycle. The variations in the dynamic responses and strength of the MCP blade during turning circle maneuvering are shown in Figure 28. The backward sweep increases blade displacement, while the forward sweep shows a more complex quadratic relationship. Blade velocity also increases slightly with the backward sweep, while it follows a quadratic trend with the forward sweep. However, the twisting angle is largely unaffected by sweep angle variations. The stress on the blade during the turning circle maneuver is moderate and stays within the safe limits of the blade material (Figures 29 and 30). The von Mises stress follows the same trend as observed in other maneuvers, being minimal at a 2° sweep angle and increasing in both forward and backward directions. The twisting moment increases with the backward sweep and decreases with the forward sweep, similar to cruising maneuvers. The normal force contributing to thrust, similar to that in other maneuvers, decreases with increasing sweep angle in both directions but remains higher in the backward sweep. This can be explained by the varying angles of attack on different blade sections at different sweep angles.

From the time series plot, we can infer that stress fluctuations are less significant compared to crash stop because of changes in the steadier flow conditions during controlled course changes. The stress distribution pattern, shown in Figure 31, exhibits variation along the blade but with a lower stress range (5–40 MPa) compared to crabbing and crash stop. In conclusion, turning circle, similar to cruising, induces moderate forces, displacements, and stresses on the MCP blade. The blade operates within safe stress limits during course changes, highlighting the dependence of these demands on the specific ship maneuvering task.

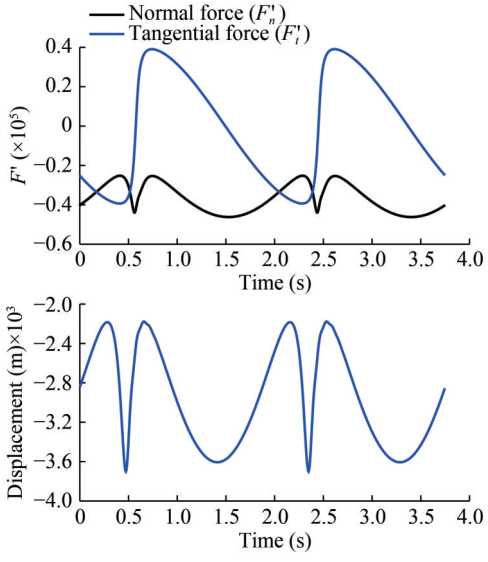

Figure 28 Nondimensionalized hydrodynamic normal and tangential forces acting on the MCP in the unswept (0° sweep angle) condition during turning circle maneuvering

A part of this work involved studying the effect of the

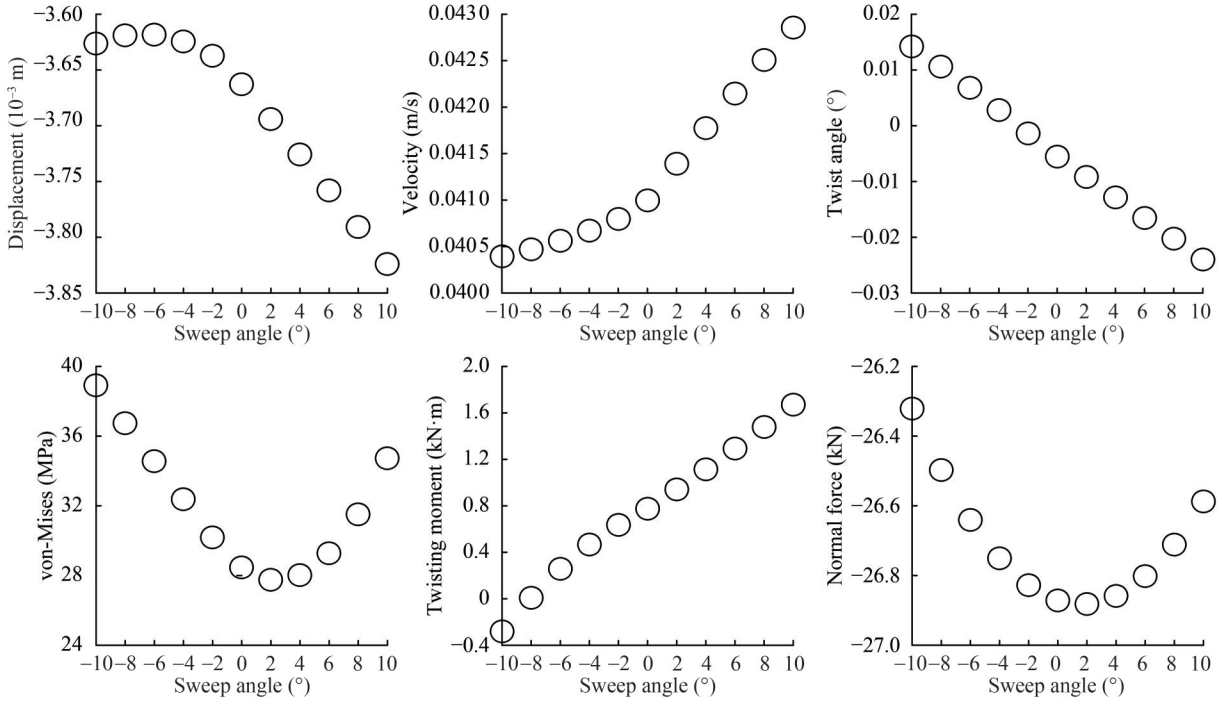

Figure 29 Variations in the maximum displacement, velocity, twist angle, twisting moment, von Mises stress, and normal force with changes in the sweep angle for the MCP during turning circle maneuvering

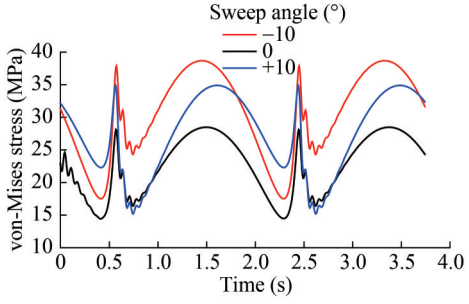

Figure 30 Time series plot of the von Mises stress at a node of the MCP blade where the maximum von Mises stress occurs at different sweep angles during turning circle maneuvering

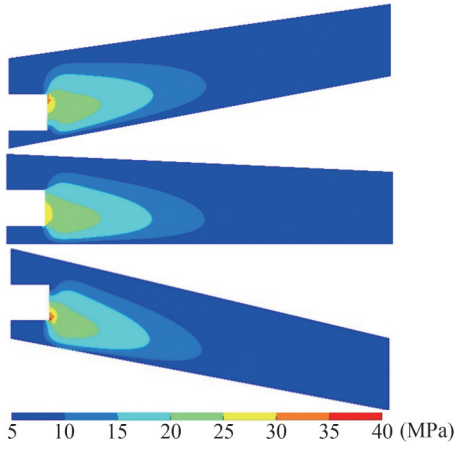

Figure 31 Contour plot of the von Mises stress on the MCP blade at the time when the maximum von Mises stress occurs during turning circle maneuvering

sweep angle on MCP blades under different ship maneuvering conditions. Table 4 briefly summarizes the overall comparison of displacement and von Mises stress under different operation conditions for extreme forward and backward sweep angles. The sweeping of blades improves flow characteristics in hydrofoils and other hydraulic machinery—it has comparable benefits for MCP blades. For most maneuvers, the von Mises stress is minimized in the unswept condition ($\theta = 0°$), indicating a more balanced load distribution and reduced structural strain. Bollard pull and crabbing maneuvers also show considerable stress but with a noticeable reduction at $\theta = 0°$. These observations suggest that maintaining a neutral sweep angle can help minimize structural stress and displacement, potentially enhancing the structural integrity and longevity of the vessel or structure being analyzed.

The above results clearly show that a fatigue analysis is crucial for cycloidal propeller blades. Although there are guidelines for assessing vibratory stresses on aircraft propellers (Federal Aviation Administraton, 2011) and marine screw propellers (DNV, 2015), few studies and guidelines pertain to MCPs. The characteristics of FSI and stress cycles for different maneuvers are listed in Tables 5 and 6, respectively. The propeller of a highly maneuverable ship is estimated to have a 25-year lifespan, with a design revolution of 32 rpm. Considering 325 working days per year, the total working lifetime is 7.020×10^8 s, and hence, the total working lifetime per maneuver will be 5.850×10^7 s. Over the course of its lifetime, the ship is expected to experience an equal amount of all the above-discussed maneuvers. The stainless steel material of the MCP blade has a stress amplitude limit of 200 MPa for 10^7 stress cycles. Among the maneuvers, crash stop experiences a high stress amplitude, reaching the material limit. Hence, high-

Table 4 Overall analysis of the maximum displacement at the leading edge of the blade and the von Mises stress at the blade stock position for −10°, 0°, and +10° sweep angles

Maneuvering	Displacement (10^{-3} m)			von Mises stress (MPa)		
	$\theta = -10°$	$\theta = 0°$	$\theta = +10°$	$\theta = -10°$	$\theta = 0°$	$\theta = +10°$
Bollard pull	−8.48	−8.66	−8.98	86	65	85
Crabbing	−5.64	−5.74	−5.96	61	45	54
Crash stop	−24.4	−25	−26	277	211	213
Cruising	−3.71	−3.74	−3.91	40	29	35
Turning circle	−3.63	−3.66	−3.83	39	28	35

Table 5 Summary of the characteristics of fluid–structure interaction

Maneuver	$(V_R)_{\text{Max}}$ (m/s)	Peak blade vibration velocity $(\lvert \dot{w}_{\text{Max}} \rvert)$ (m/s)	$\left(\frac{\lvert \dot{w}_{\text{Max}} \rvert}{(V_R)_{\text{Max}}} \times 100\right)$ (%)	$\left(\frac{\lvert w_{\text{Max}} \rvert}{R} \times 100\right)$ (%)	Peak angle of attack (from dynamics) (°)
Bollard pull	6.876	0.299	4.348	0.498	47
Crash stop	10.413	1.089	10.458	1.444	76
Cruising	10.412	0.021	0.202	0.217	6
Crabbing	6.909	0.025	0.362	0.333	30
Turning circle	10.515	0.040	0.380	0.222	18

strength material should be used. Also, an accurate estimate of the operating hours of this maneuver should be considered for fatigue assessment. Note that the 3D-BEM method gives highly accurate measurements of hydrodynamic forces. Instead of a uniform distribution, considering the variation of hydrodynamic force along the span will be more accurate when considering the structural vibration. Also, considering materials such as composites instead of structural steel can enhance propeller efficiency since composites have good strength-to-weight ratios. These aspects will be considered in future work.

Table 6 Summary of stress cycle characteristics.

Maneuver	Stress amplitude. von Mises (MPa)	Expected stress cycles in lifetime
Bollard pull	86	3.120×10^7
Crash stop	277	3.120×10^7
Cruising	40	3.120×10^7
Crabbing	61	3.120×10^7
Turning circle	39	3.120×10^7

5 Conclusions

The integration of the 3D-BEM with the FEM in this study represents an advancement over previous approaches (Prabhu et al., 2023) that relied on empirical formulas for calculating hydrodynamic forces on MCP blades. The 3D-BEM approach offers highly accurate estimates of hydrodynamic forces by considering the variations in these forces along the blade span. This is critical for capturing the complex FSI interactions between the blade and fluid, which are pronounced during maneuvers such as crash stop and crabbing. Additionally, the detailed analysis of sweep angles in this study provides new insights into optimizing blade design for improved structural integrity and performance. A MATLAB code for BEM−FEM analysis was developed for this purpose. Key parameters such as displacement, velocity, twisting angle, twisting moment, and von Mises stress were examined. The results highlight the importance of considering different maneuvering conditions during MCP blade design and operation. The principal conclusions are as follows:

1) Sweep angle notably affects the propeller responses and reactions during various ship maneuvering conditions. The MCP blade experiences greater displacement and velocity during the backward sweep than during the forward sweep. This result indicates greater response and vibration of the MCP blade when it is tilted in the direction of flow. During crash stop maneuvering at −10° backward sweep angle, the maximum displacement and velocity were 0.026 and 1.09 m/s, respectively.

2) The twisting angle of the blade increases progressively with both backward and forward sweep angles. This shows that the amount of twist experienced by the MCP blade increases almost linearly with the sweep angle. During crash stop maneuvering, the maximum twist angle was 0.16° clockwise at a backward sweep of 10°.

3) The von Mises stress at the blade support increases with the sweep angle. The maximum von Mises stress values during bollard pull, crabbing, crash stop, cruising, and turning circle maneuvers were 86, 61, 277, 40, and 39 MPa, respectively. The von Mises stress is more pronounced in the forward sweep. In crash stop maneuvers, the stress contour was in the range of 50–277 MPa.

4) The twisting moment increases with the backward sweep and decreases with the forward sweep. The peak twisting moments recorded during bollard pull, crabbing, crash stop, cruising, and turning circle maneuvers were 3.89, 2.61, 11, 1.69, and 1.67 kN·m, respectively. Notably, the blade encountered the highest twisting moment during the crash stop maneuver. Additionally, the rate of change of twisting angle with sweep angle was comparatively lower during crabbing, cruising, and turning circle maneuvers for the backward sweep.

5) The normal force magnitude on the blade decreases as the sweep angle increases across all maneuvering conditions. There exists a quadratic relationship between the sweep angle and the normal force on the blade, with greater normal force values observed in backward sweep configurations. Notably, the highest normal force of 179 kN and the highest tangential force of 206 kN are experienced during crash stop maneuvering.

6) The peak-to-peak stress variations in MCP blades decrease in the following order: crash stop, bollard pull, crabbing, cruising, and turning circle. Each maneuver exhibits a unique stress variation pattern. During the crash stop maneuver, the stress amplitude can reach the fatigue strength limit of stainless steel. For cycloidal propeller blades, both FSI interaction and fatigue loading are critical considerations, necessitating detailed analysis for efficient blade and blade stock design.

Nomenclature

A	Exposed area of the blade
C_D	Coefficient of drag
C_L	Coefficient of lift
c	Chord length of the blade
D	Drag force
e_1	Eccentricity distance in Y direction from the propeller center
e_2	Eccentricity distance in the X direction from the propeller center
g	Acceleration due to gravity

I_x, I_z	Moment of inertia of the ship about "x" and "y" axes, respectively
J	Advance coefficient
J_x, J_z	Added mass moment of inertia of the ship about "x" and "y" axes, respectively
K_P	Roll moment due to the propeller
K_W	Roll moment due to wind
L	Lift force
L_{PP}	Ship length between perpendiculars
m	Mass of the ship
m_x	Added mass in the X direction of the ship
m_y	Added mass in the Y direction of the ship
N	Number of panels
N_P	Yaw moment due to the propeller
N_W	Yaw moment due to wind
p	Roll velocity at midship
r	Yaw velocity at midship
R	Radius of the propeller disc
Re	Reynolds number based on chord length and inflow
T	Ship draft
th	Thickness of the hydrofoil section
u	Surge velocity at midship
U	Inflow velocity
V_R	Onset flow to the blade
v	Sway velocity at the midship
$X_{D\{P\}}^{\{S\}}$	Distance of the propeller disc center from midship in the X direction
X_p	Surge force due to the propeller
X_W	Surge force due to wind
$Y_{D\{P\}}^{\{S\}}$	Distance of the propeller disc center from midship in the Y direction
Y_P	Sway force due to the propeller
Y_W	Sway force due to wind
α	Angle of attack to the blade
δ_B	Blade pitch angle
$\beta_{D\{P\}}^{\{S\}}$	Blade orbit angle of the starboard and port propeller
ϕ	Angle between the eccentricity point and the normal of the blade chord
ψ	Heading angle of the ship
$\omega_{D\{P\}}^{\{S\}}$	Rotational speed of the starboard and port propeller
ρ	Density of water

Competing interest The authors have no competing interests to declare that are relevant to the content of this article.

REFERENCES

Akcabay DT, Young YL (2020) Material anisotropy and sweep effects on the hydroelastic response of lifting surfaces. Composite Structures 242: 112140. https://doi.org/10.1016/j.compstruct.2020.112140

ANSYS Inc (2023) ANSYS Mechanical (Version 2023 R1) [Computer software]. ANSYS Inc. https://www.ansys.com

Blair M, Weisshaar TA (1982) Swept composite wing aeroelastic divergence experiments. Journal of Aircraft 19(11): 1019-1024. https://doi.org/10.2514/3.44806

Čupr P, Rudolf P, Habán V (2018) Numerical investigation of added mass and damping effects on a hydrofoil in cavitation tunnel. Proceeding of 20. Internationales Seminar Wasserkraftanlagen. https://doi.org/10.1007/s35147-019-0216-2

Dash A, Nagarajan V, Sha OP (2012) Uncertainty analysis for ship maneuvering in model scale and full scale measurements. International Journal of Innovative Research and Development 1 (10): 428-448

De La Torre O, Escaler X, Egusquiza E, Farhat M (2013) Experimental investigation of added mass effects on a hydrofoil under cavitation conditions. Journal of Fluids and Structures 39: 173-187. https://doi.org/10.1016/j.jfluidstructs.2013.01.008

DNV GL Class Guideline (2015) Calculation of marine propellers, DNVGL-CG-0039, December

Ducoin A, Young YL (2013) Hydroelastic response and stability of a hydrofoil in viscous flow. Journal of fluids and structures 38: 40-57. https://doi.org/10.1016/j.jfluidstructs.2012.12.011

Federal Aviation Administration (2011) US Department of Transportation, Propeller vibration and fatigue, advisory circular

Garg N, Kenway GK, Martins JR, Young YL (2017) High-fidelity multipoint hydrostructural optimization of a 3-D hydrofoil. Journal of Fluids and Structures 71: 15-39. https://doi.org/10.1016/j.jfluidstructs.2017.02.001

Ghassemi H, Yari E (2011) The added mass coefficient computation of sphere, ellipsoid and marine propellers using boundary element method. Polish Maritime Research 18(1): 17-26. https://doi.org/10.2478/v10012-011-0003-1

ITTC (2011) Proceedings. 26th International Towing Tank Conference, Rio de Janeiro, Brazil

Katz J, Plotkin A (2001) Low-speed aerodynamics (Vol. 13). Cambridge University Press

Kim YJ, Lee HY, Lee CS (2008) The added mass and damping for the axial rigid body motion of a marine propeller rotating in a uniform flow. Journal of the Society of Naval Architects of Korea 45(3): 309-314. DOI: 10.3744/SNAK. 2008. 45. 3. 309

Li J, Qu Y, Chen Y, Hua H (2018) Investigation of added mass and damping coefficients of underwater rotating propeller using a frequency-domain panel method. Journal of Sound and Vibration 432: 602-620. https://doi.org/10.1016/j.jsv.2018.06.060

Liao Y, Martins JR, Young YL (2019) Sweep and anisotropy effects on the viscous hydroelastic response of composite hydrofoils. Composite Structures 230: 111471. https://doi.org/10.1016/j.compstruct.2019.111471

Lottati I (1985) Flutter and divergence aeroelastic characteristics for composite forward swept cantilevered wing. Journal of Aircraft 22(11): 1001-1007. https://doi.org/10.2514/3.45238

Nandy S, Nagarajan V, Sha OP (2022) Model experiments with different cycloidal propeller algorithms using same electric controller. Proceedings of the Institution of Mechanical Engineers, Part M: Journal of Engineering for the Maritime Environment 236(2): 436-461. https://doi.org/10.1177/1475090221103634

Nandy S, Nagarajan V, Sha OP (2018) On the heuristic based

electronic control of marine cycloidal propeller. Applied Ocean Research 78: 134-155. https://doi.org/10.1016/j.apor.2018.05.013

Ozdemir YH, Barlas B (2021) 2D and 3D potential flow simulations around NACA 0012 with ground effect. Research Square. DOI: 10.21203/rs.3.rs-151154/v1

Pica A, Wood RD, Hinton E (1980) Finite element analysis of geometrically nonlinear plate behaviour using a mindlin formulation. Computers & Structures 11(3): 203-215. https://doi.org/10.1016/0045-7949(80)90160-1

Prabhu JJ, Dash AK, Nagarajan V, Sha OP (2019) On the hydrodynamic loading of marine cycloidal propeller during maneuvering. Applied Ocean Research 86: 87-110. https://doi.org/10.1016/j.apor.2019.02.008

Prabhu JJ, Dash AK, Nagarajan V, Sunny MR (2023) Vibration analysis of cycloidal propeller blade during ship maneuvering. Journal of Marine Science and Technology 28(1): 44-71. https://doi.org/10.1007/s00773-022-00899-1

Prabhu JJ, Nagarajan V, Sunny MR, Sha OP (2017) On the fluid structure interaction of a marine cycloidal propeller. Applied Ocean Research 64: 105-127. https://doi.org/10.1016/j.apor.2017.01.019

Rabczuk T, Zi G, Bordas S, Nguyen-Xuan H (2010) A simple and robust three-dimensional cracking-particle method without enrichment. Computer Methods in Applied Mechanics and Engineering 199: 2437-2455. https://doi.org/10.1016/j.cma.2010. 03.031

Wang X, Zhang Y, Wen M, Mang HA (2025) A simple hybrid linear and nonlinear interpolation finite element for the adaptive Cracking Elements Method. Finite Elements in Analysis and Design 244: 104295. https://doi.org/10.1016/j.finel.2024.104295

Zhang Y, Huang J, Yuan Y, Mang HA (2021) Cracking elements method with a dissipation-based arc-length approach. Finite Elements in Analysis and Design 195: 103573. https://doi.org/10.1016/j.finel.2021.103573

Zhang Y, Zhuang X (2019) Cracking elements method for dynamic brittle fracture. Theoretical and Applied Fracture Mechanics 102: 1-9. https://doi.org/10.1016/j.tafmec.2018.09.015

Zienkiewicz OC, Taylor RL, Taylor RL (2000) The finite element method: solid mechanics (2) Butterworth-heinemann